# Observation of chiral zero mode in inhomogeneous three-dimensional Weyl metamaterials

Jia, Hongwei; Zhang, Ruixing; Gao, Wenlong; Guo, Qinghua; Yang, Biao; Hu, Jing; Bi, Yangang; Xiang, Yuanjiang; Liu, Chaoxing; Zhang, Shuang

*DOI:*
10.1126/science.aau7707

# Observation of chiral zero mode in inhomogeneous 3D Weyl metamaterials

**Authors:** Hongwei Jia,[1,2] Ruixing Zhang,[3,4] Wenlong Gao,[1] Qinghua Guo,[1,2] Biao Yang,[1] Jing Hu,[1] Yangang Bi,[1] Yuanjiang Xiang,[2]* Chaoxing Liu,[3]* Shuang Zhang[1]*

**Affiliations:**

[1]School of Physics and Astronomy, University of Birmingham, Birmingham B15 2TT, UK.

[2]International Collaborative Laboratory of 2D Materials for Optoelectronic Science & Technology of Ministry of Education, College of Optoelectronic Engineering, Shenzhen University, Shenzhen 518060, China.

[3]Department of Physics, The Pennsylvania State University, University Park, Pennsylvania 16802-6300, USA.

[4]Condensed Matter Theory Center and Joint Quantum Institute, Department of Physics, University of Maryland, College Park, Maryland 20742, USA.

*Correspondence to: yjxiang@szu.edu.cn (Y.X.); cxl56@psu.edu (C.L.); s.zhang@bham.ac.uk (S.Z.)

**Abstract:** Due to the chirality of Weyl nodes, the Weyl systems can support one-way chiral zero modes under a strong magnetic field, which lead to nonconservation of chiral currents – the so called chiral anomaly. While promising for robust transport of optical information, the zero chiral bulk modes have not been observed in photonics. Here we design an inhomogeneous Weyl metamaterial in which a gauge field is generated for the Weyl nodes by engineering the individual unit cells. We experimentally confirm the presence of the gauge field and observe the zero order chiral Landau level with one-way propagation. Without breaking the time-reversal symmetry, our system provides a route for designing artificial magnetic field in 3D photonic Weyl systems, and may have potential for device applications in photonics.

**One Sentence Summary:** A Weyl metamaterial with artificial magnetic field gives rise to zeroth chiral Landau level in the bulk.

**Main Text:** Three dimensional (3D) Dirac and Weyl (*1-12*) semimetals are topological phases of matter that support relativistic quasi-particles near the degeneracy points between two bands. Weyl points are two-fold band crossings with topological charges (or chiralities) (*3,4*), whose existence requires breaking time-reversal (TR) or inversion (I) symmetry of the Dirac system (*5,13*). As a Weyl point has a co-dimension 3=3-0, it is highly robust and cannot be eliminated unless two partners with opposite chiralities annihilate each other in *k*-space (*3,14*). Due to the band crossings resulting from accidental degeneracy, the positions of Weyl points can be designed by introducing structural change in the unit cells (*14*). These properties provide us a good opportunity for engineering gauge fields (artificial magnetic field) by designing the spatially-dependent displacement of Weyl points in the *k*-space.

Mechanical strain has been introduced to generate gauge field especially in 2D systems. Within the tight binding approximation, the strain tensor can be written in the form of the vector potential. Artificial magnetic field has been generated in 2D crystal lattice by strains (*15-20*). However, in 3D bulk crystals, artificial magnetic fields cannot be generated readily because these systems are not flexible. Thus research has concentrated on geometries such as films or wires to explore relevant effect induced by strains (*21*). Because of this limitation, artificially induced gauge fields have only been realized in 2D systems. Artificial magnetic field in 3D Weyl systems is expected to exhibit additional intriguing properties such as chiral transport of Weyl fermions.

In high energy physics, the chiral anomaly describes a phenomenon that the conservation law of the chirality (left-handed or right-handed) for the particles or waves is broken down when external electric and magnetic fields are applied in parallel in 3D Weyl systems (*22*). It was proposed that the chiral transport may be observed in crystals that support Weyl fermions (*23*). By applying an ordinary (*24-26*) or an artificial magnetic field (e.g. external strain) (*21,27,28*) to a Dirac or Weyl system, Dirac types of Landau levels can be formed. In particular, a special type of zeroth Landau level is expected to propagate only in the chiral (left or right) direction that is determined by the chirality of the corresponding Weyl points and the magnetic field direction. The presence of chiral zeroth Landau levels in Dirac/Weyl systems is the physical origin of chiral transport, which has been experimentally tested through the negative magnetoresistance in electronic systems (*29-31*). Recently, various 3D electronic (*1,3,4*) and photonic systems (*2,6-12*) that support Dirac or Weyl degeneracies were discovered, providing a platform for experimentally detecting chiral zeroth Landau levels. However, the photonic counterpart has not been explored yet.

We experimentally realize an artificial magnetic field by designing inhomogeneous photonic structures based on the recently discovered ideal Weyl metamaterial (*8*). To engineer the photonic gauge field in 3D Weyl metamaterial, we must spatially vary the location of the Weyl points in *k*-space. The designed metamaterial has a hexahedron unit cell (3mm×3mm×4.5mm) (Fig. 1A), and each unit cell consists of a saddle-shaped connective metallic coil. The structure possesses four Weyl degeneracy points on the $k_z$=0 plane (*8*). Here, through elaborate design of each individual unit cell at different locations, we introduce adiabatic variation of the unit cell structure to realize fine control over the locations of the Weyl points in the *k*-space, and meanwhile keeping the frequency of the Weyl points unchanged (Fig. 1A). The current distribution in the saddle-shaped coil can be solved with the LC circuit model. Using the effective medium approach (*32*), the constitutive parameters can be obtained [see Section 4 in (*33*)]. Specifically, the angle $\theta$ causes the angular shift of the Weyl points about the Γ point [see

Section 5 and Fig. S3 in (*33*)], whereas the offset *d* between the metal strip and the center of the via hole is carefully tuned to maintain the Weyl frequency.

The metamaterial consists of metallic coils with spatially variant rotational angles [Fig. 1B, Section 6 and Fig. S4 in (*33*) for the whole structure], with a uniform angular step $\Delta\theta$=0.2° between adjacent unit cells along the *x* direction, while the translational symmetry in the *y* and *z* directions are maintained. This leads to a linear relation $\theta=ax$ *rad*, with $a=-2\pi\times10^2/3/180$ (*rad*/*m*). The metamaterial has 101 unit cells in the *x* direction, so that the rotational angle $\theta$ ranges from 10° to -10° from one end to the other end. The offset parameter *d* has been adapted to ensure the Weyl points are located at the same frequency everywhere in the structure. To confirm the positions of the Weyl points in the *k*-space, the band structure is calculated with CST Microwave studio (Fig. 1C for $\theta$=0). The system supports four Type I Weyl points (Q1-Q4). In the vicinity of each Weyl point, the effective Hamiltonian can be written as (*4*)

$$H_W = \mathbf{w}\cdot(\mathbf{k}-\mathbf{k}_0^W)\sigma_0 + \sum_{i,j=x,y,z} v_{ij}(k_i - k_{0,i}^W)\sigma_j, \quad (1)$$

where $\sigma_j$ are the Pauli matrices, $\sigma_0$ is the 2×2 identity, $v_{ij}$ is the element of an anisotropic velocity tensor, and $\mathbf{k}_0^W$ denotes the location of the Weyl point in the *k*-space. Here the identity $\sigma_0$ is introduced into the Hamiltonian to describe the tilt of the cone-like dispersion near the degeneracy point (Fig. 1C). By rotating the metallic coil with a small angle $\theta$, the four Weyl points rotate the same angle $\theta$ around $k_z$ axis simultaneously, leading to a displacement of the position of the Weyl point (see Fig. 1D, taking the Weyl point Q1 in Fig. 1C as an instance) $\Delta k_x^W \approx \theta k_0^W/\sqrt{2}$, $\Delta k_y^W \approx -\theta k_0^W/\sqrt{2}$. The changes of velocity components in the effective Hamiltonian are almost negligible if $\theta$ is small [Section 7 and Table S2 in (*33*)]. One can simply derive a new Hamiltonian that characterizes the overall system, $H_W \approx \mathbf{w}\cdot(\mathbf{k}-\mathbf{k}_0^W-\mathbf{A})\sigma_0 + \sum v_{ij}(k_i - k_{0i}^W - A_i)\sigma_i$. Since $\theta$ is a linear function of the spatial coordinate *x*, one can approximately define the gauge field as the position shift of the Weyl point $\mathbf{A}=\Delta\mathbf{k}^W \approx [axk_0^W/\sqrt{2}, -axk_0^W/\sqrt{2}, 0]^{\mathrm{T}}$. The artificial magnetic field can thus be obtained by $\mathbf{B}=\nabla\times\mathbf{A}$ to be $\mathbf{B}=[0,0,-ak_0^W/\sqrt{2}]^{\mathrm{T}}$.

To confirm the existence of the gauge field in the system, we employ a near field scanning technique (Fig. 2A), with the excitation point source located at five different positions along the *x* direction on the bottom surface (labeled by 1, 2, …, 5). For each location of the excitation source, a detector scans across the overall top surface to obtain the electric field distribution. With a discrete Fourier transform, the distribution of field amplitude in the *k*-space can be obtained. The detected signal intensity in the *k*-space strongly relies on the source position, where the local eigen states are strongly excited. Thus, it is expected that with the increase of *x*, the four Weyl points are shifted in the *k*-space following the blue arrows in Fig. 2B, with the direction of the generated gauge field for each Weyl point along *z* or –*z* direction as indicated by the right panel of Fig. 2B. Figure 2C shows the experimental results corresponding to different source locations at a frequency of 13.48GHz, which is higher than the Weyl frequency. Note that this selected frequency is outside the energy gap between the two 1st order Landau levels, so as to avoid the impact of chiral zero modes. It is seen that the four Weyl points rotates around the $k_z$ axis at the four excitation locations, confirming the existence of the spatially dependent pseudo-gauge field. For comparison, we plot the corresponding numerical results of

Weyl point positions in Fig. 2D, which are consistent with the experimental results. The gauge fields for each Weyl node are estimated based on the experimental results, which show reasonably good agreement with the simulation result, which is about 477 $m^{-2}$ [see Section 8 in (*33*)].

Chiral zeroth Landau levels for relativistic particles can be generated in 3D Dirac or Weyl systems when external or artificial magnetic field is applied (*21,25-28*). Our designed inhomogeneous Weyl metamaterial with artificial magnetic field provides an ideal platform for observing the photonic counterpart of chiral zero modes. The dispersions of Landau levels are expressed as [see Section 9 in (*33*) for deriving details]

$$\omega_n = \begin{cases} w_z k_z \pm \dfrac{\sqrt{v_\perp^{\,2} - w_\perp^{\,2}}}{v_\perp} \sqrt{v_z^2 k_z^2 + 2nBv_\perp \sqrt{v_\perp^{\,2} - w_\perp^{\,2}}}, & n > 0 \\ [w_z + \chi^z \mathrm{sgn}(B) \dfrac{v_z \sqrt{v_\perp^{\,2} - w_\perp^{\,2}}}{v_\perp}] k_z, & n = 0 \end{cases}, \qquad (2)$$

where $v_\perp$ and $w_\perp$ are rescaled velocities taking into account the tilt of the cone-like dispersion near the Weyl points (*33*), $w_z = 0$ for our sample, and $\chi^z$ is the chirality of each Weyl point. The Landau levels are calculated by Eq. (2) and presented in Figs. 3A and 3B. Determined by both the directions of the artificial magnetic fields (Fig. 2B) and the chiralities of Weyl points [Table S5 in (*33*)], the zeroth Landau levels in two Weyl points Q3 and Q4 (Figs. 3A, C) have the group velocities in the positive *z* direction. In contrary, Weyl points Q1 and Q2 (Figs. 3B, C) have chiral zero modes with group velocity in the negative *z* direction. The group velocities of zeroth Landau levels at these four Weyl points (Q1-Q4) respect both time reversal and mirror symmetry [see symmetry analysis in Section 9 of (*33*)]. For an excitation point source located on the bottom surface (Fig. 3D), it is expected that only the up-propagating zeroth Landau levels in Q3 and Q4 can be excited and detected on the top surface. Due to the conservation of the in-plane momentum, the reflection at the top surface cannot couple to down-going Landau levels in Q1 and Q2. In the experiments, the Fourier transform of the field patterns on the top surface shows that the Weyl points Q3 and Q4 are much more pronounced than Q1 and Q2 in the vicinity of the Weyl frequency [(E3-E5) in Fig. 3]. Within the gap formed between the first order Landau levels, the ratio between the measured intensities of the up-going Landau and that of the down-going Landau levels exceeds 5 [Section 10 and Fig. S9 in (*33*)]. However, if the source frequency is far from the Weyl frequency [(E1-E2 and E6-E7) in Fig. 3], the four Weyl points are almost equally excited. On the contrary, for the point source located on the top surface (Fig. 3F), Weyl points Q1 and Q2 are more strongly excited than Q3 and Q4 [(G3-F5) in Fig. 3] close to the Weyl frequency, while at other frequencies [(G1-G2 and G6-G7) in Fig. 3], all four Weyl points are equally excited. Thus, our experiments directly confirm chiral propagation of the zeroth Landau levels in Weyl systems. We further confirm the robust transport of the zero chiral modes against reflection by inserting a defect layer of dielectric slab or air in the middle of the sample and measuring the amplitude of the transmitted bulk modes [Section 11 and Fig. S10 in (*33*)].

We have designed an inhomogeneous Weyl metamaterial in which the positions of the Weyl points in the *k*-space are dependent on the spatial coordinate. The observed shift of the Weyl point positions is equivalent to a pseudo-gauge field (or an artificial magnetic field) in the

system. The ability to design the Weyl metamaterial provide a route for generating artificial magnetic field in 3D photonic systems, and provides an ideal platform for exploring novel topological phenomena enabled by strong magnetic fields (*21,25-28*). The chiral zeroth Landau level, which is a one way propagative bulk mode, can be applied for robust transport of photons in the bulk medium.

Note added: During the review of our paper we noticed a recent work which claimed demonstration of chiral zero mode in acoustic systems (*34*).

**References and Notes:**

1. Z. K. Liu, B. Zhou, Y. Zhang, Z. J. Wang, H. M. Weng, D. Prabhakaran, S.-K. Mo, Z. X. Shen, Z. Fang, X. Dai, Z. Hussain, Y. L. Chen, Discovery of a three-dimensional topological Dirac semimetal, Na3Bi. *Science* **343**, 864-867 (2014).
2. Q. Guo, B. Yang, L. Xia, W. Gao, H. Liu, J. Chen, Y. Xiang, S. Zhang, Three dimensional photonic Dirac points in metamaterials. *Phys. Rev. Lett.* **119**, 213901 (2017).
3. X. Wan, A. M. Turner, A. Vishwanath, S. Y. Savrasov, Topological semimetal and Fermi-arc surface states in the electronic structure of pyrochlore iridates. *Phys. Rev. B* **83**, 205101 (2011).
4. A. A. Soluyanov, D. Gresch, Z. Wang, Q. S. Wu, M. Troyer, Xi Dai, B. A. Bernevig, Type-II Weyl semimetals. *Nature* **527**, 495 (2015).
5. L. Lu, L. Fu, J. D. Joannopoulos, M. Soljačić, Weyl points and line nodes in gyroid photonic crystals. *Nat. Photonics* **7**, 294 (2013).
6. L. Lu, Z. Wang, D. Ye, L. Ran, L. Fu, J. D. Joannopoulos, M. Soljačić, Experimental observation of Weyl points. *Science* **349**, 622-624 (2015).
7. B. Yang, Q. Guo, B. Tremain, L. E. Barr, W. Gao, H. Liu, B. Béri, Y. Xiang, D. Fan, A. P. Hibbins, S. Zhang, Direct observation of topological surface-state arcs in photonic metamaterials. *Nat. Commun*. **8**, 97 (2017).
8. B. Yang, Q. Guo, B. Tremain, R. Liu, L. E. Barr, Q. Yan, W. Gao1, H. Liu, Y. Xiang, J. Chen, C. Fang, A. Hibbins, L. Lu, S. Zhang, Ideal Weyl points and helicoid surface states in artificial photonic crystal structures. *Science* **359**, 1013-1016 (2018).
9. N. P. Armitage, E. J. Mele, A. Vishwanath, Weyl and Dirac semimetals in three-dimensional solids. *Rev. Mod. Phys.* **90**, 015001 (2018).
10. W.-J. Chen, M. Xiao, C. T. Chan, Photonic crystals possessing multiple Weyl points and the experimental observation of robust surface states. *Nat. Commun.* **7**, 13038 (2016).
11. M. Dubois, C. Shi, X. Zhu, Y. Wang, X. Zhang, Observation of acoustic Dirac-like cone and double zero refractive index. *Nat. Commun.* **8**, 14871 (2017).
12. A. Slobozhanyuk, S. H. Mousavi, X. Ni, D. Smirnova, Y. S. Kivshar, A. B. Khanikaev, Three-dimensional all-dielectric photonic topological insulator. *Nat. Photonics* **11**, 130 (2017).
13. L. Lu, J. D. Joannopoulos, M. Soljačić, Topological photonics. *Nat. Photonics* **8**, 821 (2014).

14. A. Weststrom, T. Ojanen, Designer curved-space geometry for relativistic fermions in Weyl metamaterials. *Phys. Rev. X* **7**, 041026 (2017).

15. F. Guinea, M. I. Katsnelson, A. K. Geim, Energy gaps and a zero-field quantum Hall effect in graphene by strain engineering. *Nat. Phys.* **6**, 30-33 (2010).

16. J. L.Manes, Symmetry-based approach to electron-phonon interactions in graphene. *Phys. Rev. B* **76**, 045430 (2007).

17. M.C. Rechtsman, J. M. Zeuner, A. Tünnermann, S. Nolte, M.Segev, A. Szameit, Strain-induced pseudomagnetic field and photonic Landau levels in dielectric structures. *Nat. Photonics* 7, 153 (2012).

18. N. Levy, S. A. Burke, K. L. Meaker, M. Panlasigui, A. Zettl, F. Guinea, A. H. Castro Neto, M. F. Crommie, Strain-induced pseudo–magnetic fields greater than 300 tesla in graphene nanobubbles. *Science* **329**, 544-547 (2010).

19. G. Salerno, T. Ozawa, H. M. Price, I. Carusotto, How to directly observe Landau levels in driven-dissipative strained honeycomb lattices. *2D Mater.* **2**, 034015 (2015).

20. H. Abbaszadeh, A. Souslov, J. Paulose, H. Schomerus, V. Vitelli, Sonic Landau levels and synthetic gauge fields in mechanical metamaterials. *Phys. Rev. Lett.* **119**, 195502 (2017).

21. D. I. Pikulin, A. Chen, M. Franz, Chiral anomaly from strain-induced gauge fields in Dirac and Weyl semimetals. *Phys. Rev. X* **6**, 041021 (2016).

22. J. M. Ziman, *Principles of the Theory of Solids*. (Cambridge,1972).

23. H. B. Nielsen, N. Masao, The Adler-Bell-Jackiw anomaly and Weyl fermions in a crystal. *Phys. Lett. B* **130**, 389-396 (1983).

24. Z. M. Yu, Y. Yao, S. A. Yang, Predicted unusual magnetoresponse in type-II Weyl semimetals. *Phys. Rev. Lett.* **117**, 077202 (2016).

25. S. Tchoumakov, M. Civelli, M. O. Goerbig, Magnetic-field-induced relativistic properties in type-I and type-II Weyl semimetals. *Phys. Rev. Lett.* **117**, 086402 (2016).

26. X. Yuan, Z. Yan, C. Song, M. Zhang, Z. Li, C. Zhang, Y. Liu, W. Wang, M. Zhao, Z. Lin, T. Xie, J. Ludwig, Y. Jiang, X. Zhang, C. Shang, Z. Ye, J. Wang, F. Chen, Z. Xia, D. Smirnov, X. Chen, Z. Wang, H. Yan, F. Xiu, Chiral Landau levels in Weyl semimetal NbAs with multiple topological carriers. *Nat. Commun.* **9**, 1854 (2018).

27. A. G. Grushin, J. W. F. Venderbos, A. Vishwanath, R. Ilan, Inhomogeneous Weyl and Dirac semimetals: Transport in axial magnetic fields and Fermi arc surface states from pseudo-Landau levels. *Phys. Rev. X* **6**, 041046 (2016).

28. C. X. Liu, P. Ye, X. L. Qi, Chiral gauge field and axial anomaly in a Weyl semimetal. *Phys. Rev. B*, **87**, 235306 (2013)

29. D. T. Son, B Z. Spivak, Chiral anomaly and classical negative magnetoresistance of Weyl metals. *Phys. Rev. B* **88**, 104412 (2013).

30. X. Huang, L. Zhao, Y. Long, P. Wang, D. Chen, Z. Yang, H. Liang, M. Xue, H. Weng, Z. Fang, X. Dai, G. Chen, Observation of the chiral-anomaly-induced negative magnetoresistance in 3D Weyl semimetal TaAs. *Phys. Rev. X* **5**, 031023 (2015).

31. Z. M. Yu, Y. Yao, S A. Yang, Predicted unusual magnetoresponse in type-II Weyl semimetals. Phys. Rev. Lett. **117**, 077202 (2016).

32. R. Zhao, T. Koschny, C. M. Soukoulis, Chiral metamaterials: retrieval of the effective parameters with and without substrate. *Opt. Express* **18**, 14553-14567 (2010).

33. Materials and methods are available as supplementary materials.

34. V. Peri, M. Serra-Garcia, R. Ilan, S. D. Huber, Axial field induced chiral channels in an acoustic Weyl system. arXiv preprint arXiv:1806.09628 (2018).

**Acknowledgments:** This work was financially supported by the European Research Council Consolidator Grant (Topological), Horizon 2020 Action Project grant 734578 (D-SPA). S.Z. acknowledges support from the Royal Society and Wolfson Foundation. Y. X. acknowledges support from the National Natural Science Foundation of China (Grant Nos. 61490713 and 11604216). C.X. L acknowledges the support from Office of Naval Research (Grant No. N00014-15-1-2675). **Funding:** European Research Council Consolidator Grant (Topological), Horizon 2020 Action Project grant 734578 (D-SPA), National Natural Science Foundation of China (Grant No. 61490713 and 11604216); Office of Naval Research under Grant No. N00014-15-1-2675; **Author contributions:** HJ, YX, CL and SZ planned the project. HJ, YX, WG, QG, and BY contributed to the design of the metamaterial. HJ, QG, JH, YB carried out the measurement. HJ, RZ, WG, YX, CL and SZ analyzed the data and performed the theoretical modeling. HJ, CL and SZ wrote the manuscript. All authors contributed to the discussion; **Competing interests:** Authors declare no competing interests; and **Data and materials availability:** All data is available in the main text or the supplementary materials.

**Supplementary Materials:**

Materials and Methods

Figures S1-S10

Tables S1-S5

References (*8,21,25-32*)

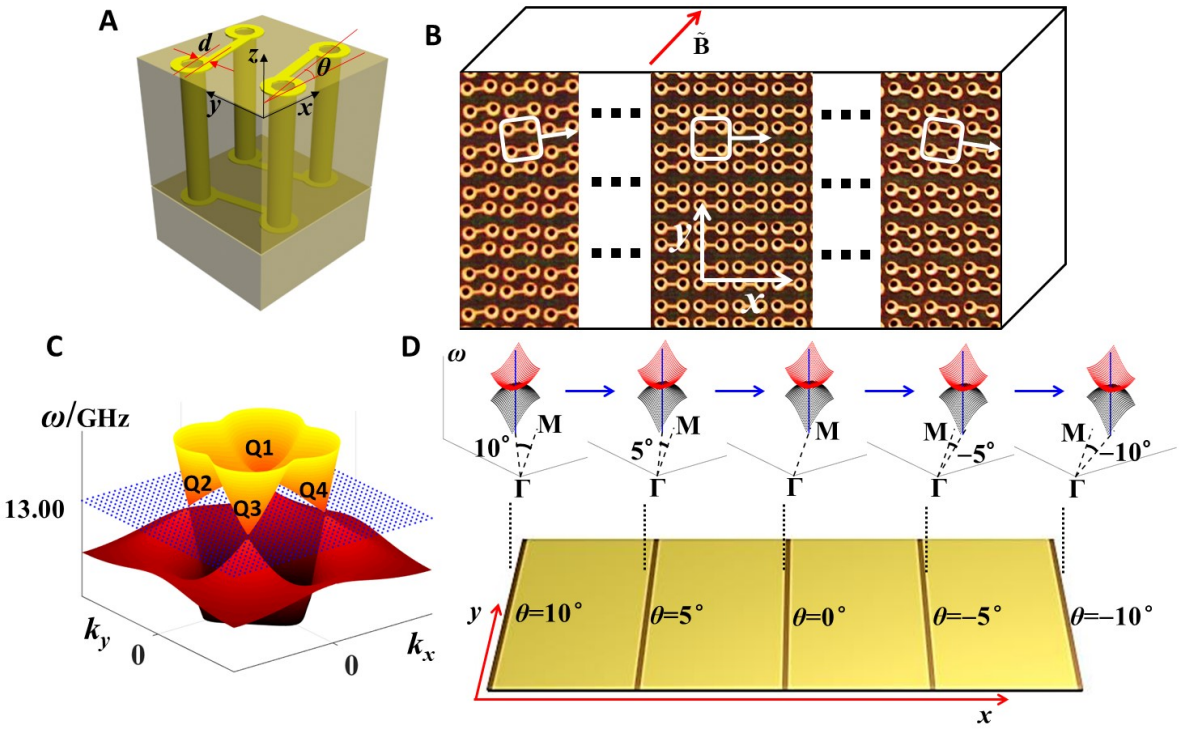


**Fig. 1. Structure and dispersion of the inhomogeneous Weyl metamaterial.** (A) Schematic of the saddle-shaped metallic coil, whose rotational angle $\theta$ and offset distance $d$ between the center of the via and the metal strip can be varied to tune the positions and the frequency of the Weyl points. The metallic structure is embedded in a dielectric (dielectric constant 2.2) block with dimension 3mm×3mm×4.5mm. (B) Photograph of the top surface of the sample. The rotational angle $\theta$ has a linear gradient in $x$, with a variation from positive to negative with a uniform step $\Delta\theta$=0.2° between adjacent unit cells along $x$ direction. The sample has 101 unit cells both in $x$ and $y$ directions, and the rotational angle $\theta$ ranges from 10° to -10°. (C) Dispersion diagram of the Weyl metamaterial with $\theta$=0, four tilted type I Weyl cones labeled by Q1-Q4 are located in different quadrants. The result is calculated with CST Microwave Studio (D) CST simulated results of the position shift of the Weyl point Q1 as the spatial coordinate $x$ varies. The angle of the connection of Weyl point with Γ point relative to Γ-M connection varies simultaneously with the rotational angle $\theta$ from 10° to -10°.

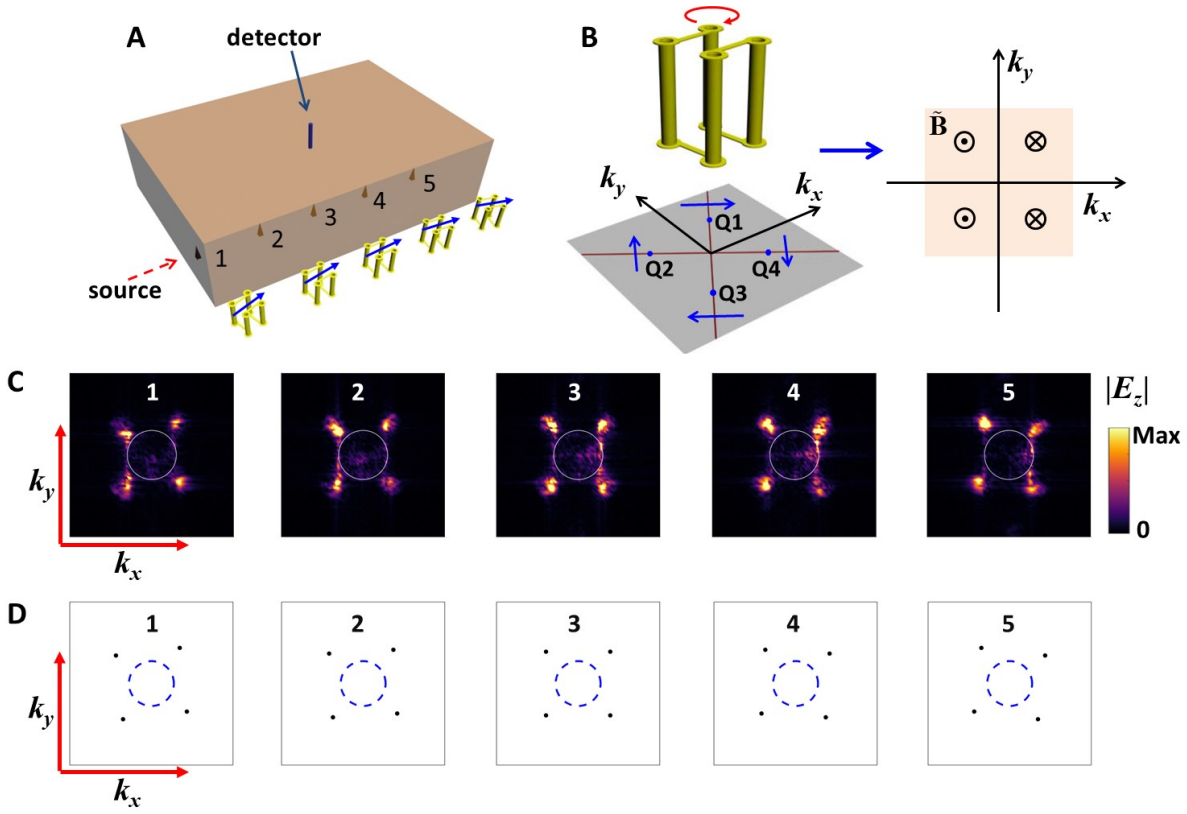


**Fig. 2. Pseudo-gauge field generated by the spatially dependent rotational angle $\theta$.** (A) Experimental setup for detecting gauge field. The source is located at five different positions on the bottom surface as labeled from 1 to 5. (B) Shifting of the locations of Weyl points (left panel) and the directions of artificial magnetic field (right panel). The blue arrows denote the shifting direction of the Weyl points Q1-Q4 as $x$ coordinate (or rotational angle $\theta$) varies. The spatial shift of the Weyl points is equivalent to the presence of a gauge field. (C) Equi-frequency contour $|E_z|$ measured using setup (A) at frequency 13.48GHz, with panels 1-5 corresponding to the results for source located at 1-5 in (A). (D) Numerical results of Weyl point positions with 5 panels corresponding to the five locations in (A). Results are calculated by CST microwave studio.

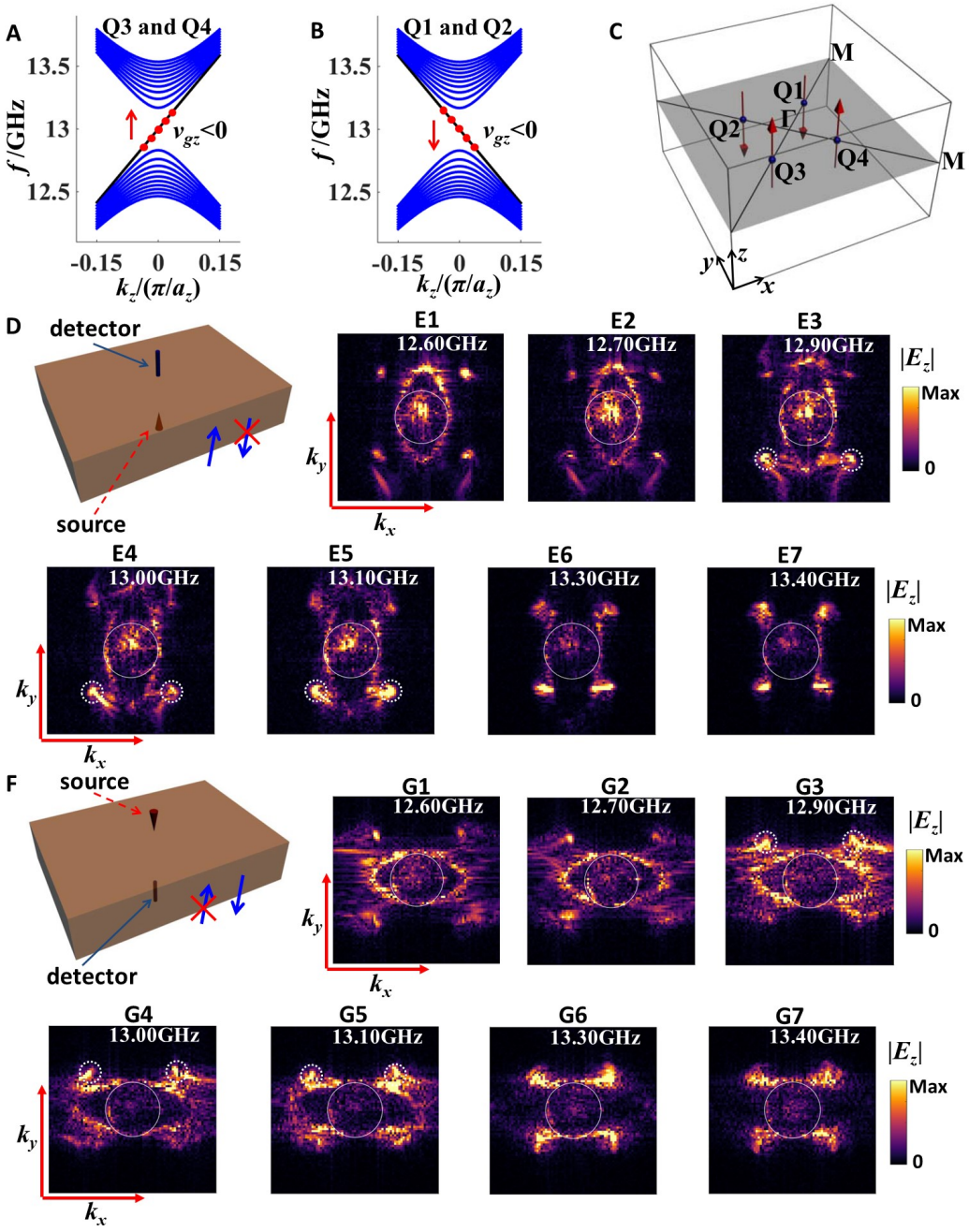


**Fig. 3. Chiral zero mode in inhomogeneous Weyl metamaterial**. (A and B) Band structures of Landau levels for Weyl points Q3 and Q4 and Weyl points Q1 and Q2 respectively, with $a_z$ being the side length of unit cell in $z$ direction. The group velocities of chiral zero modes in (A) and (B) are along opposite directions. (C) Chiral transport of Weyl photons for Weyl points Q1-Q4. The red arrows indicate the direction of group velocity at each Weyl point. (D and F) Experimental setups for detecting down-going and up-going chiral zero modes, respectively. The source is located on the upper center and bottom center respectively. (E and G) Equi-frequency contours ($|E_z|$) measured by setups (D) and (F). Panels 1-7 correspond to different frequencies.

Two Weyl points surrounded by white dashed circles are much stronger excited than the other two in panels C3-C5 and F3-F5, at those frequencies close to the Weyl frequency.